# Golden Palladium Zinc Ordered Intermetallics as Oxygen Reduction Electrocatalysts

Yao Yang,<sup>†,‡,||</sup> Weiping Xiao,<sup>†,||</sup> Xinran Feng,<sup>‡,§</sup> Yin Xiong,<sup>‡</sup> Mingxing Gong,<sup>†</sup> Tao Shen,<sup>†</sup> Yun Lu,<sup>†</sup> Héctor D. Abruña, in and Deli Wang\*, in

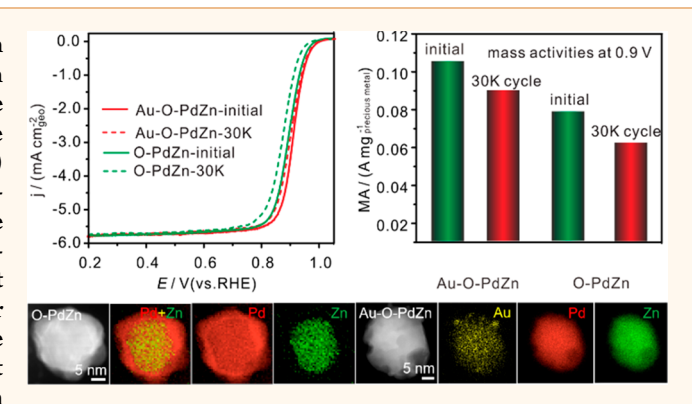
<sup>†</sup>Key laboratory of Material Chemistry for Energy Conversion and Storage, Ministry of Education; Hubei Key Laboratory of Material Chemistry and Service Failure, School of Chemistry and Chemical Engineering, Huazhong University of Science and Technology, Wuhan 430074, China

\*Department of Chemistry and Chemical Biology, Baker Laboratory, Cornell University, Ithaca, New York 14853, United States §Cornell High Energy Synchrotron Source (CHESS), Cornell University, Ithaca, New York 14853, United States

Supporting Information

Downloaded via CORNELL UNIV on March 31, 2020 at 17:05:26 (UTC). See https://pubs.acs.org/sharingguidelines for options on how to legitimately share published articles.

ABSTRACT: Exploring Pt-free electrocatalysts with high activity and long durability for the oxygen reduction reaction (ORR) has been long pursued by the renewable energy materials community. In this work, we have designed an ordered intermetallic PdZn/C (O-PdZn) with a several atomic-layer Pd shell, which achieved a 3fold enhancement in ORR mass activities (MA) in alkaline media, relative to Pd/C and Pt/C. Further Au incorporation in O-PdZn/C (Au-O-PdZn/C) yielded a catalyst with superior durability with less than 10% loss in MA after 30000 potential cycles. These effects have attributed to the rationally designed ordered structure and stabilizing effect of Au atoms. Aberration-corrected scanning transmission



electron microscopy and synchrotron-based X-ray fluorescence spectroscopy were employed to show that Au not only galvanically replaced Pd and Zn on the surface but also penetrated through the PdZn lattice and distributed uniformly within the particles. Au-O-PdZn/C was also tested as an effective oxygen cathode in broad applications in rechargeable Li-air and Zn-air batteries.

**KEYWORDS:** fuel cell, metal—air battery, oxygen reduction reaction, ordered intermetallics, Pt-free electrocatalysts

ydrogen fuel cells have been recognized as crucial renewable energy technologies to power electrical vehicles (EVs) due to their high energy density, high energy-conversion efficiency, and potential zero carbon emission.<sup>1,2</sup> However, a significant amount of Pt (>0.2 g/ kW) is still required to catalyze the sluggish ORR for a power density of >1 W/cm<sup>2,2-7</sup> Alternatively, Pd has shown ORR activity comparable to Pt in alkaline media.8 To further enhance the ORR activity, tremendous efforts have been devoted to alloying Pd with much lower-cost 3d-transition metals. 9-13 However, the reported Pd-based alloys are often disordered alloys and suffer from rapid leaching of the 3dtransition metals, which can severely contaminate and degrade the membrane in fuel cells.<sup>2,14</sup> Pt, Pd-based intermetallics, with ordered structures, have been reported to effectively mitigate the leaching problem and exhibit enhanced durability. 5-7,15-24 In this work, we have designed a structurally ordered Auincorporated (golden) PdZn (Au-O-PdZn) intermetallic with high initial ORR activity and long-term durability.

# **RESULTS AND DISCUSSION**

Disordered PdZn (D-PdZn/C), synthesized by an impregnation method, exhibited a typical face-centered cubic (fcc) structure as shown in the X-ray diffraction (XRD) pattern in Figure 1a. The peak positions of PdZn/C were shifted to higher angles, relative to Pd/C, indicating a lattice contraction due to the incorporation of Zn. After a postannealing treatment at 500 °C, the XRD pattern exhibited the characteristic (001) and (100) peaks of an ordered intermetallic PdZn (O-PdZn) phase. Compared with Pd/C, the lattice parameter of D-PdZn contracted by 1.23%, while that of O-PdZn contracted by 11.0% in the c direction and expanded by 5.45% in the a and b directions (Table S1).

The crystal structure of O-PdZn/C was then examined, at the atomic scale, by a STEM operated at 300 kV (Figures 1b

Received: March 12, 2019 Accepted: April 18, 2019 Published: April 18, 2019

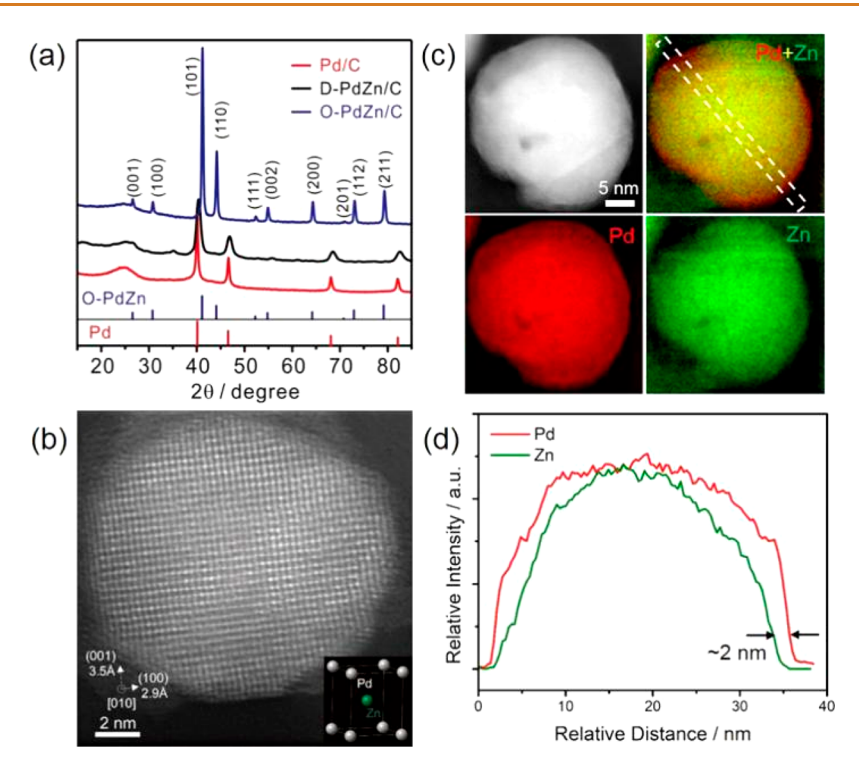


Figure 1. (a) Powder XRD patterns of Pd/C and disordered and ordered PdZn/C (D-PdZn/C and O-PdZn/C). (b) Atomic-scale HAADF-STEM image of O-PdZn/C on the [010] zone axis. Inset: PdZn unit cell. (c) STEM image and the corresponding EELS elemental maps of Pd, Zn, and Pd vs Zn. (d) EELS line scan profile extracted from the dashed box in (c), indicating a  $\sim$ 2 nm Pd shell.

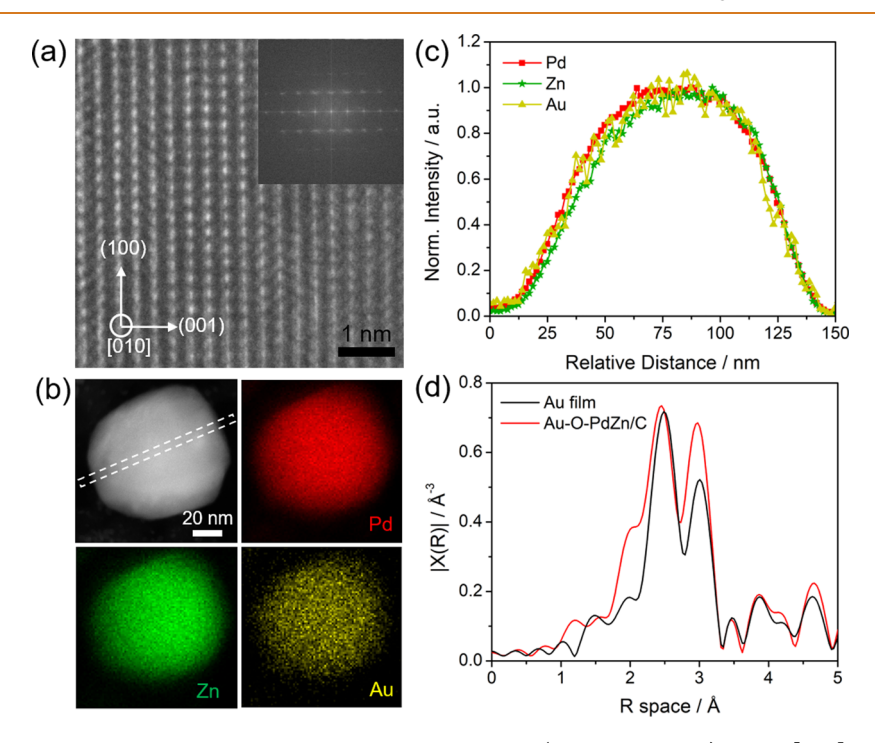


Figure 2. (a) Atomic-scale HR-TEM image of Au-incorporated ordered PdZn/C (Au-O-PdZn/C) on the [010] zone axis. (b) STEM image and the corresponding EDX elemental maps of Pd, Zn, and Au. (c) EDX line scan profile of Pd, Zn, and Au, extracted from the dashed box in (b). (d) FT-EXAFS spectra of Au-O-PdZn and Au film reference.

and S1). The low-magnification high-angle annular dark-field (HAADF) STEM images of ordered PdZn/C in Figure S2 exhibited a narrow size distribution with an average size of ca. 50 nm, which is consistent with the domain size calculated from XRD patterns (Figure 1a). The atomic-scale STEM image in Figure 1b visualized the ordered intermetallic

structure of PdZn along the [010] zone axis. Two perpendicular lattice planes were assigned to be the (100) (2.9 Å) and (001) (3.5 Å), which were consistent with the theoretical values of 2.9 and 3.4 Å, respectively (ordered PdZn, PDF No. 01-072-2936). Since the intensity of HAADF-STEM images is proportional to the atomic number (I  $\alpha$  Z<sup>1.7</sup>), the

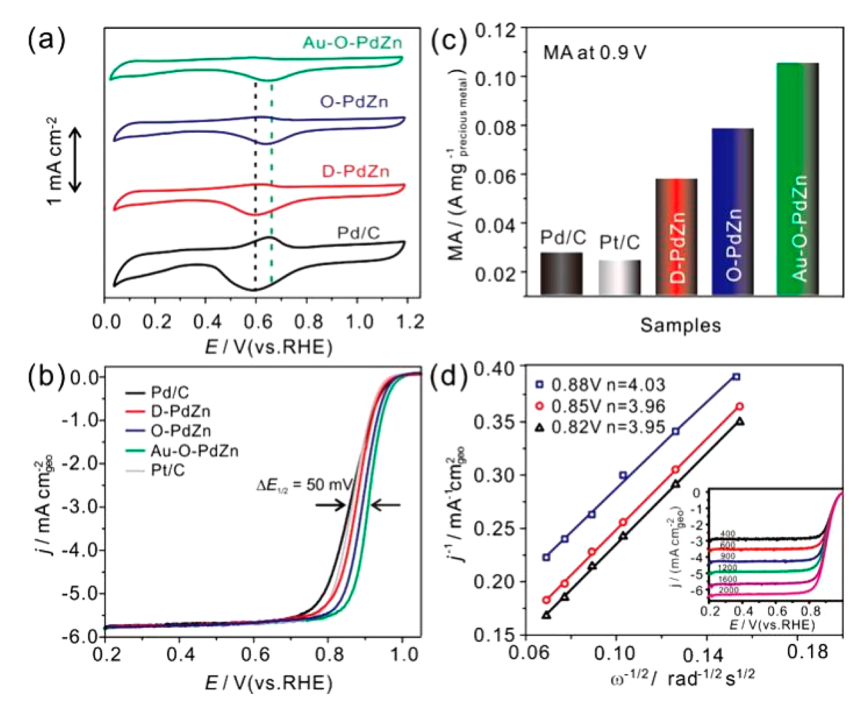


Figure 3. (a) CV profiles of Pd/C, D-PdZn/C, O-PdZn/C, and Au-O-PdZn/C at 50 mV/s in Ar-saturated 0.1 M KOH. (b) ORR polarization profiles of Pd/C, Pt/C, D-PdZn/C, O-PdZn/C, and Au-O-PdZn/C at 5 mV/s and 1600 rpm in O<sub>2</sub>-saturated 0.1 M KOH. The mass loadings of precious metal were 40  $\mu$ g cm<sup>-2</sup>. (c) Mass activities (MA) of different catalysts at 0.9 V vs RHE. (d) Koutecky-Levich plots of Au-O-PdZn at different potentials. Inset: I-V curves at various rotation rates.

atom columns clearly showed a periodic rectangular array of brighter Pd atom columns surrounding the dimmer Zn atom columns in the center. The chemical composition of O-PdZn/C was further investigated using electron energy loss spectroscopy (EELS) elemental mapping. Figure 1c shows another PdZn nanoparticle with (101) lattice planes (2.2 Å) and the corresponding EELS elemental maps of Pd and Zn (Figure S3). The Pd (red) vs Zn (green) composite map indicated that the PdZn core (yellow) was surrounded by a thin Pd shell (red). The line profiles in Figure 1d, corresponding to the dashed boxes in Figure 1c, indicated that the thickness of the Pd shell is about 2 nm. This five to six atomic layer Pd-rich shell, on the surface, may serve as a protection shell to mitigate Zn leaching and improve the electrocatalytic durability.

The incorporation of Au into Pd-based alloys has been demonstrated to greatly improve the long-term durability of ORR electrocatalysts. 14,15,25,26 A galvanic replacement method was utilized to partially replace the Pd and Zn with Au atoms. PdZn/C was able to maintain the ordered structure after incorporating Au, as shown by the XRD patterns in Figure S4. The ordered structure of Au-incorporated O-PdZn/C (Au-O-PdZn) was then examined using bright-field high-resolution TEM (HR-TEM) imaging. Figure 2a indicated an ordered intermetallic particle of Au-O-PdZn on the [010] zone axis, similar to that of O-PdZn in Figure 1. Given the low Au content in Au-O-PdZn (Au/Pd = 1:40) and the nature of fully occupied 5d<sup>10</sup> orbitals of Au, the EELS signal-to-noise ratio of Au M<sub>4,5</sub> edges was below the detection limit. Alternatively, energy-dispersive X-ray (EDX) spectroscopy was employed as a reliable tool to acquire a convincing Au elemental map from the Au L $\beta$  edge (Figure S5). Au-O-PdZn/C exhibits a homogeneous elemental distribution of Au and Pd based on the corresponding EDX elemental maps (Figure 2b). EDX

elemental line profiles (Figure 2c), extracted from dashed boxes in Figure 2b, show that Au has similar bell-shaped line profiles as Pd and Zn, suggesting that Au is uniformly distributed through the entire particle. If Au only existed on the surface of PdZn, it would show a plateau in the middle of the line scan profile, rather than a bell-shaped line.  $^{6,10,27}$  EDX line profiles of Au-O-PdZn/C also suggest a thin Pd shell of 2-3 nm, which is similar to the EELS mapping results of O-PdZn/C. EDX mapping has a lower spatial resolution relative to EELS due to the larger beam size in order to collect enough X-ray signals. The incorporation of Au was further examined by the Fourier-transformed extended X-ray absorption fine structure (FT-EXAFS). As shown in Figure 2d, the first shell peak at around 2.5 Å shifted to a shorter R with respect to that of the Au film references, which is likely due to partial charge transfer from Pd and Zn to Au, since Au has a higher Pauling electronegativity (2.54) than Pd (2.20) and Zn (1.65). The peak splitting at 2.75 Å is due to the Ramsauer-Townsend effect on the Fr(k) function.<sup>28</sup> In summary, the microscopiclevel EDX and macroscopic-level FT-EXAFS analyses strongly indicate that Au atoms are uniformly incorporated into the ordered PdZn lattice.

After detailed structural investigations, the electrocatalytic ORR activities were evaluated with a rotating disk electrode (RDE) in  $O_2$ -saturated 0.1 M KOH solution at 1600 rpm. Cyclic voltammetric (CV) profiles (Figure 3a) exhibit the oxide reduction peak of D-PdZn/C, O-PdZn, and Au-O-PdZn gradually shifted to higher potentials (dashed lines in Figure 3a), compared with Pd/C, indicating that PdZn alloying and further Au-decoration could weaken the oxygen affinity and improve the ORR activity. The ORR polarization profiles indicated that the half-wave potential ( $E_{1/2}$ ) of O-PdZn, D-PdZn, and Au-O-PdZn shifted positively by 20, 34, and 50 mV, respectively, relative to those of Pd/C and Pt/C (Figure 3b).

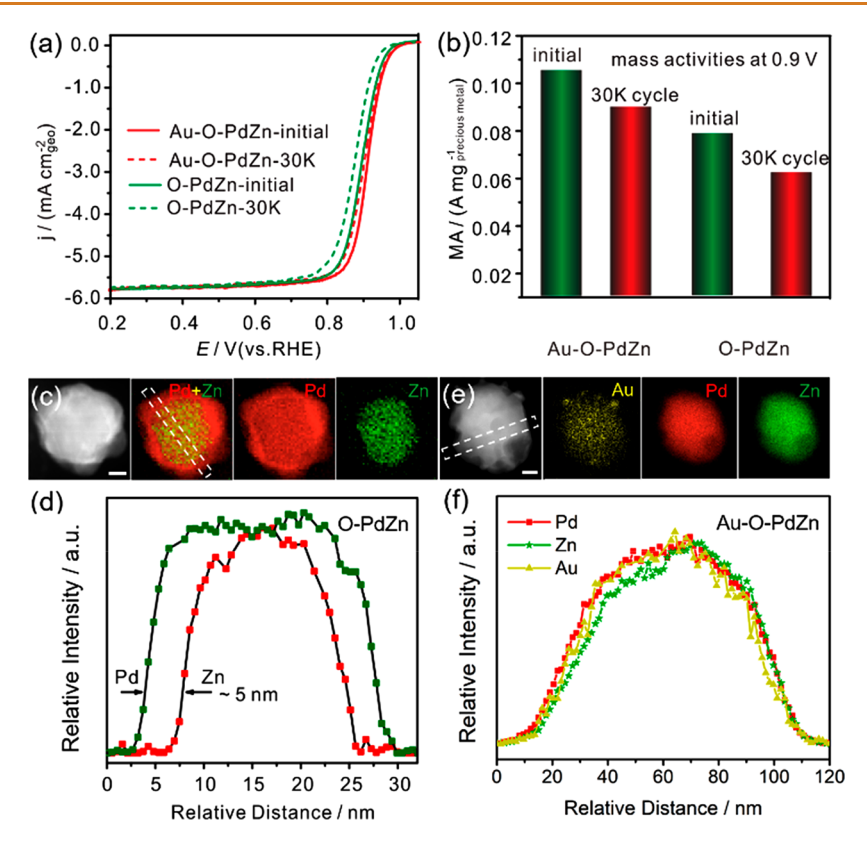


Figure 4. (a, b)ORR polarization profiles of Au-O-PdZn and O-PdZn catalysts before and after 30000 cycles and the corresponding MA. (c) STEM image of O-PdZn after 30K cycles and the corresponding EELS elemental maps of Pd and Zn and the composite map of Pd vs Zn. Scale bar: 5 nm. (d) EELS line profiles extracted from the dashed box in (c). (e) STEM image of Au-O-PdZn after 30 K electrochemical cycles and the corresponding EDX elemental maps of Au, Pd, and Zn. Scale bar: 20 nm. (f) EDX line scan profile extracted from the dashed box in (e).

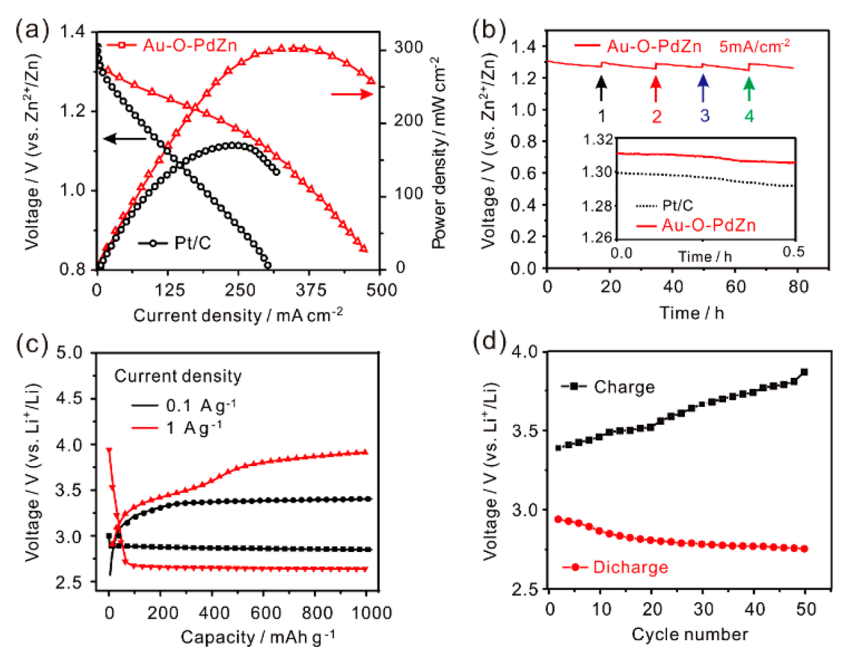


Figure 5. Cell performance of Zn-air batteries using Pt/C and Au-O-PdZn catalysts as cathodes. (b) Durability test at 5 mA/cm<sup>2</sup>. Zn-air batteries were supplied with fresh Zn foil every 20 h as labeled 1-4. (c) Cell performance of Li-air batteries using Au-O-PdZn/C as the cathode at current densities of 0.1 and 1 A  $\rm g^{-1}$ . (d) Long-term discharge/charge profiles of Au-O-PdZn at 0.1 A  $\rm g^{-1}$  with a capacity of 1000 mAh  $\rm g^{-1}$  per cycle in Li-air batteries.

Furthermore, based on the mass loading of Pd and Au, the mass activity (MA) of Au-O-PdZn/C was calculated to be 0.105~A/mg at 0.9~V, significantly higher than that of D-PdZn/

C (0.056~A/mg) and O-PdZn/C (0.078~A/mg) as well as Pt/C and Pd/C (Figure 3c). The electron-transfer number of Au-O-PdZn was calculated to be nearly 4.0, according to the

Koutecky-Levich equation, indicating a minimal peroxide formation (Figure 3d).

The electrocatalytic durability was then examined by performing accelerated potential cycling from 0.6 to 1.0 V (Figure 4). The  $E_{1/2}$  of Au-O-PdZn decreased by 6 mV after 30000 cycles, while O-PdZn exhibited a larger decay of 13 mV (Figure 4a). The MA of Au-O-PdZn/C decreased by 9.5%, relative to a 16.6% decay for O-PdZn/C (Figure 4b). To gain a microscopic-level understanding of the catalyst degradation mechanism, the morphology and chemical composition of catalysts were examined using STEM. As shown in Figure S6, although some particles aggregated into large nanoparticles (Figure S6a), the ordered structure was well preserved as shown by the selected area electron diffraction (SAED) pattern which exhibited the characteristic features of ordered PdZn, comparable to the XRD pattern in Figure 1a. The HR-TEM image of O-PdZn/C after electrochemical cycling also revealed the ordered crystal structure viewed on the [010] zone axis (Figure S6c,d). Similar to O-PdZn/C, Au-O-PdZn/C also maintained the ordered structure and experienced particle aggregation after 30000 cycles (Figure S7a-d). Interestingly, EELS elemental mapping of O-PdZn/C after cycling exhibited a thicker Pd shell of around 4 nm when compared to the 2 nm Pd shell of the as-synthesized O-PdZn/C, indicating a partial leaching of Zn after cycles. EDX elemental mapping of Au-O-PdZn/C after electrochemical cycling indicated that Au had a similar distribution profile as Pd and Zn in the same particle, similar to the initial state, indicating a stable structure of Au-O-PdZn and possibly contributing to the long-term durability (Figures 4e,f).

As a promising ORR electrocatalyst, the Au-O-PdZn/C was further tested as the oxygen cathode in proof-of-concept rechargeable metal—air batteries (Figure 5). Zn—air batteries were assembled with Au-O-PdZn/C as the cathode, zinc foil as the anode, and 6 M KOH as the electrolyte. As shown in Figure 5a, the Au-O-PdZn/C cathode exhibited a peak power density of ~310 mW cm<sup>-2</sup> at a current density of ~353 mA cm<sup>-2</sup>, which are much higher than those of a typical Pt/C cathode (~240 mA cm<sup>-2</sup> and ~175 mW cm<sup>-2</sup>, respectively). The inset in Figure 5b indicated that the Au-O-PdZn had a higher discharge plateau voltage (1.315 V) than Pt/C (1.30 V), suggesting that Au-O-PdZn/C could lower the ORR overpotential in Zn—air batteries. The Au-O-PdZn/C cathode exhibited negligible performance degradation after continuously discharging for 80 h (Figure 5b).

Inspired by previous work on bifunctional electrocatalysts in Li-air batteries, <sup>29-34</sup> The Au-O-PdZn/C was tested as a catalyst for one of the most challenging charging reactions  $(\text{Li}_2\text{O}_2 - 2\text{e}^- = 2\text{Li}^+ + \text{O}_2)$ . Au-O-PdZn/C exhibited stable discharging/charging plateaus (~2.85/3.36 V vs Li<sup>+</sup>/Li) (Figure 5c) with charging overpotentials as low as 0.38 V at 0.1 A g<sup>-1</sup>. This represents a dramatic improvement, considering that the typical charging overpotential is 0.8-1.0 V on carbon black without electrocatalysts. 30-36 When the current density was increased by a factor of 10 to 1 A g<sup>-1</sup>, the charging overpotential initially only increased to around 0.5 V at 300 mAh g<sup>-1</sup> but the charging voltage slowly rose to around  $3.8~\mathrm{V}$  at  $1000~\mathrm{mAh}~\mathrm{g}^{-1}$ , which is likely due to the slow kinetics of decomposing lithium carbonate byproducts formed during discharge.<sup>35</sup> Durability tests indicated that the Au-O-PdZn/C cathode was able to maintain fairly constant discharging/ charging plateaus within the first 20 cycles. However, larger charging overpotentials were evident in the following cycles,

which possibly came from the accumulation of nonactive byproducts, due to the electrolyte instability and carbon corrosion effects.<sup>36</sup>

#### **CONCLUSIONS**

In summary, Au-O-PdZn ordered intermetallics with a Pd shell and uniform Au distribution exhibited superior ORR activity in alkaline media and significantly enhanced durability. Moreover, Au-O-PdZn/C was used as an effective oxygen cathode in Zn—air batteries and Li—air batteries. The strategy described herein provides valuable insights to design high-performance and long-durability oxygen cathodes for both hydrogen fuel cells and rechargeable metal—air battery technologies.

## **EXPERIMENTAL METHODS**

**Material Synthesis.** The PdZn catalysts were prepared by an impregnation—reduction method. In a typical synthesis, 0.1879 mmol of PdCl<sub>2</sub> (Aldrich), 0.1879 mmol of ZnCl<sub>2</sub> (Aldrich), 67.8 mg of Vulcan, and 10 mL of deionized water were mixed, and the dispersion was then heated to 60 °C to evaporate the water under alternating magnetic stirring and sonication. Disordered PdZn/C (D-PdZn/C) catalysts were synthesized under a  $\rm H_2$  gas atomsphere at 300 °C for 2 h. D-PdZn/C was then annealed under  $\rm H_2$  gas at 500 °C for 2 h to form ordered PdZn/C (O-PdZn/C). Au was incoporated into O-PdZn/C using a galvanic replacement method (Au:Pd = 1:40) since  $\rm AuCl_4^{2-}/Au$  has a more positive redox potential (0.93 V vs the standard hydrogen electrode (SHE)) than those of PdCl<sub>4</sub><sup>2-</sup>/Pd and  $\rm Zn^{2+}/Zn$  (0.59 V,  $\rm -0.76~vs$  SHE, respectively).

Structural Characterizations. The X-ray diffraction (XRD) patterns were obtained by using an X'Pert PRO diffractometer with Cu K $\alpha$  radiation. X-ray fluorescence spectroscopy (XRF) at the Au L<sub>III</sub> edge was acquired at the C-1 beamline of the Cornell High Energy Synchrotron Source (CHESS). About one hundred XRF spectra were collected and merged to enhance the weak Au signal and compensate for the EXAFS noise caused by random photon fluctuations from the X-ray beam. XRF spectra were calibrated using Au foils (measured concurrently with the sample in transmission mode) and analyzed using the ATHENA software package. Fourier-transformed extended X-ray absorption fine structure (FT-EXAFS) spectra were processed by setting the Fourier-transformed window to be  $3-11 \text{ Å}^{-1}$  with  $k^3$ weighting and no phase correction. EXAFS of the Pd was not included because neither the Pd K edge (24.35 keV) nor the L<sub>I</sub> edge (3.6 keV) was suitable for the synchrotron source used in this work (6-15 keV).

High-angle annular dark-field (HAADF) scanning transmission electron microscopy (HAADF-STEM) images and electron energy loss spectroscopy (EELS) elemental maps were acquired using a fifthorder aberration-corrected FEI Titan Themis STEM operated at 300 kV with a beam convergence semiangle of 30 mrad and subangstrom spatial resolution. Atomic-scale STEM images were processed using the Richard-Lucy filtering method with two iterations (Figure S1). EELS spectral images were acquired with a 0.25 eV/channel energy dispersion in a Gatan spectrometer with a size of  $100 \times 100$  pixels and an acquisition time of 20 ms/pixel. The Pd and Zn EELS elemental maps were extracted using Pd M<sub>4.5</sub> and Zn L<sub>3.2</sub> edges, respectively, from EELS spectral images and processed using the linear combination of power law (LCPL) to subtract the background in ImageJ software. High-resolution TEM (HRTEM), selected area electron diffraction (SAED), and energy-dispersive X-ray spectroscopy (EDX) elemental mapping were performed using a FEI Tecnai F-20 (S)TEM operated at 200 kV. EDX elemental maps of Pd, Zn, and Au were processed using Pd L $\alpha$ , $\beta$  and Zn L $\alpha$ , and Au L $\beta$  edges, respectively. The spatial resolution of EDX mapping was estimated to be 2–3 nm based on the Goldstein equation,  $R \propto \frac{Z\sqrt{N}}{E}t^{1.5}$ , where R is the resolution and Z, N, E, and t are the atomic number, atom density, incident beam energy, and sample thickness, respectively. It should be noted that the Pd shell, in EDX mapping, was not as well resolved as

the EELS mapping due to the limitations of spatial resolution in EDX mapping (2–3 nm) when using a larger beam size, as a compromise, to achieve a higher beam current and sufficient EDX signal for Au mapping.

**Electrochemical Characterization.** Electrochemical experiments were conducted using a RDE setup with an Autolab-PGSTAT302N potentiostat in 0.1 M KOH solution. Catalyst inks were prepared by mixing 5 mg of catalyst with 1 mL of 2-propanol/Nafion (0.1% Nafion) solution. An 8  $\mu$ L catalyst ink was then deposited on the RDE electrode (5 mm in diameter, area: 0.196 cm²). All electrochemical measurements were conducted in 0.1 M KOH aqueous solution using a three-electrode cell with a reversible hydrogen electrode (RHE) as the reference electrode and a carbon rod as counter electrode. The ORR polarization profiles were measured in O<sub>2</sub>-saturated 0.1 M KOH solution from 0.2 to 1.1 V  $\nu s$  RHE at a scan rate of 5 mV s<sup>-1</sup> and a rotation rate of 1600 rpm. Durability tests were conducted by potential cycling between 0.6 and 1.0 V at a scan rate of 100 mV s<sup>-1</sup> in O<sub>2</sub>-saturated 0.1 M KOH solution.

Zn-Air and Li-Air Battery Tests. The Zn-air batteries was assembled with a layered battery. 0.2 M  $Zn(CH_3COO)_2 + 6$  M KOH was used as the electrolyte, and a polished Zn foil was used as the anode electrode. The Au-O-PdZn or Pt/C was loaded on the carbon cloth to serve as the oxygen cathode. The loading of the synthesized catalyst was 0.5 mg cm<sup>-2</sup>. A LAND-CT2001A battery test station was used at a current density of 5 mA cm<sup>-2</sup>. For the Li-air battery test, the Au-O-PdZn catalyst, carbon black (SuperP), and polymer binder (polyvinlidene fluoride; PVDF) in a weight ratio of 80:10:10 were mixed in azodimethylpyrrolidone to obtain a smooth slurry. The slurry was then loaded onto a carbon paper and dried in a vacuum oven at 80 °C for 24 h. The average loading of the Au-O-PdZn was 0.5 mg cm<sup>-2</sup>. The Li-air batteries were assembled inside a glovebox (H<sub>2</sub>O < 0.5 ppm, O<sub>2</sub> < 0.5 ppm) using Au-O-PdZn/C supported on carbon paper as the cathode, a Li metal foil as the anode, glass fiber as the separator, and LiTFSI/TEGDME as the electrolyte. The assembled battery was purged with O2 gas for 10 h to allow O2 gas fully diffuse and reach the cathode and tested under flowing O2 gas. The specific capacity was normalized to the mass of the precious metals. The charge and discharge profiles were measured at a current density of 0.1 and 1 A  $g_{catalyst}^{-1}$ . The durability test was conducted at a constant current density of 0.1 A g<sub>catalyst</sub><sup>-1</sup> and a capacity of 1000 mAh g<sub>catalyst</sub><sup>-1</sup> per cycle for 50 cycles.

## **ASSOCIATED CONTENT**

# S Supporting Information

The Supporting Information is available free of charge on the ACS Publications website at DOI: 10.1021/acsnano.9b01961.

Figures S1-S7 and Tables S1-S2 (PDF)

# **AUTHOR INFORMATION**

#### **Corresponding Author**

\*E-mail: wangdl81125@hust.edu.cn.

ORCID ®

Yao Yang: 0000-0003-0321-3792

Héctor D. Abruña: 0000-0002-3948-356X

Deli Wang: 0000-0003-2023-6478

## **Author Contributions**

Y.Y. and W.X. contributed equally.

### **Notes**

The authors declare no competing financial interest.

## **ACKNOWLEDGMENTS**

This work was supported by the National Natural Science Foundation (21573083), 1000 Young Talent (to D.W.), and the Innovation Research Funds of Huazhong University of Science and Technology (2017KFYXJJ164). We thank the

Analytical and Testing Center of Huazhong University of Science & Technology for allowing us to use its facilities for XRD measurements. This work made use of TEM facilities at the Cornell Center for Materials Research (CCMR) which are supported through the National Science Foundation Materials Research Science and Engineering Center (NSF MRSEC) program (DMR-1719875). We are grateful to Malcolm (Mick) Thomas at CCMR for the help with Nion UltraSTEM. This work is based upon research conducted at the Cornell High Energy Synchrotron Source (CHESS), which is supported by the National Science Foundation under Award No. DMR-1332208. We greatly appreciate the assistance of CHESS staff scientists K. Finkelstein and C. Pollock.

#### **REFERENCES**

- (1) Debe, M. K. Electrocatalyst Approaches and Challenges for Automotive Fuel Cells. *Nature* **2012**, 486, 43–51.
- (2) Gasteiger, H. A.; Kocha, S. S.; Sompalli, B.; Wagner, F. T. Activity Benchmarks and Requirements for Pt, Pt-alloy, and non-Pt Oxygen Reduction Catalysts for PEMFCs. *Appl. Catal., B* **2005**, *56*, 9–35
- (3) Xiong, Y.; Yang, Y.; Joress, H.; Padgett, E.; Gupta, U.; Yarlagadda, V.; Agyeman-Budu, D. N.; Huang, X.; Moylan, T. E.; Zeng, R.; Kongkanand, A.; Escobedo, F. A.; Brock, J. D.; DiSalvo, F. J.; Muller, D. A.; Abruña, H. D. Revealing the Atomic Ordering of Binary Intermetallics Using *In Situ* Heating Techniques at Multilength Scales. *Proc. Natl. Acad. Sci. U. S. A.* **2019**, *116*, 1974–1983.
- (4) Wang, D.; Xin, H. L.; Hovden, R.; Wang, H.; Yu, Y.; Muller, D. A.; DiSalvo, F. J.; Abruña, H. D. Structurally Ordered Intermetallic Platinum-Cobalt Core-Shell Nanoparticles with Enhanced Activity and Stability as Oxygen Reduction Electrocatalysts. *Nat. Mater.* **2013**, *12*, 81–87.
- (5) Xiong, Y.; Yang, Y.; DiSalvo, F. J.; Abruña, H. D. Pt-Decorated Composition-Tunable Pd-Fe@Pd/C Core-Shell Nanoparticles with Enhanced Electrocatalytic Activity toward the Oxygen Reduction Reaction. *J. Am. Chem. Soc.* **2018**, *140*, 7248–7255.
- (6) Yang, Y.; Wang, Y.; Xiong, Y.; Huang, X.; Shen, L.; Huang, R.; Wang, H.; Pastore, J. P.; Yu, S.-H.; Xiao, L.; Brock, J. D.; Zhuang, L. & Abruña, H. D. *In situ* X-ray Absorption Spectroscopy of a Synergistic Co–Mn Oxide Catalyst for the Oxygen Reduction Reaction. *J. Am. Chem. Soc.* **2019**, *141*, 1463–1466.
- (7) Xiong, Y.; Yang, Y.; Feng, X.; DiSalvo, F. J.; Abruña, H. D. A Strategy for Increasing the Efficiency of the Oxygen Reduction Reaction in Mn-Doped Cobalt Ferrites. *J. Am. Chem. Soc.* **2019**, *141*, 4412–4421.
- (8) Lima, F.; Zhang, J.; Shao, M.; Sasaki, K.; Vukmirovic, M.; Ticianelli, E.; Adzic, R. Catalytic Activity—d-Band Center Correlation for the O<sub>2</sub>Reduction Reaction on Platinum in Alkaline Solutions. *J. Phys. Chem. C* **2007**, *111*, 404–410.
- (9) Jiang, G.; Zhu, H.; Zhang, X.; Shen, B.; Wu, L.; Zhang, S.; Lu, G.; Wu, Z.; Sun, S. Core/Shell Face-Centered Tetragonal FePd/Pd Nanoparticles as an Efficient Non-Pt Catalyst for the Oxygen Reduction Reaction. *ACS Nano* **2015**, *9*, 11014–11022.
- (10) Wang, D.; Xin, H. L.; Wang, H.; Yu, Y.; Rus, E.; Muller, D. A.; DiSalvo, F. J.; Abruña, H. D. Facile Synthesis of Carbon-supported Pd—Co Core—shell Nanoparticles as Oxygen Reduction Electrocatalysts and Their Enhanced Activity and Stability with Monolayer Pt Decoration. *Chem. Mater.* **2012**, *24*, 2274—2281.
- (11) Xiao, W.; Cordeiro, M. A. L.; Gong, M.; Han, L.; Wang, J.; Bian, C.; Zhu, J.; Xin, H. L.; Wang, D. Optimizing the ORR Activity of Pd Based Nanocatalysts by Tuning Their Strain and Particle Size. *J. Mater. Chem. A* **2017**, *5*, 9867–9872.
- (12) Luo, L.; Zhu, F.; Tian, R.; Li, L.; Shen, S.; Yan, X.; Zhang, J. Composition-Graded  $Pd_xNi_{1-x}$  Nanospheres with Pt Monolayer Shells as High-Performance Electrocatalysts for Oxygen Reduction Reaction. ACS Catal. **2017**, 7, 5420–5430.

(13) Shao, M.; Shoemaker, K.; Peles, A.; Kaneko, K.; Protsailo, L. Pt Monolayer on Porous Pd-Cu Alloys as Oxygen Reduction Electrocatalysts. *J. Am. Chem. Soc.* **2010**, *132*, 9253–9255.

- (14) Kongkanand, A.; Subramanian, N. P.; Yu, Y.; Liu, Z.; Igarashi, H.; Muller, D. A. Achieving High-Power PEM Fuel Cell Performance with an Ultralow-Pt-Content Core-Shell Catalyst. *ACS Catal.* **2016**, *6*, 1578–1583.
- (15) Wang, D.; Liu, S.; Wang, J.; Lin, R.; Kawasaki, M.; Rus, E.; Silberstein, K. E.; Lowe, M. A.; Lin, F.; Nordlund, D.; Liu, H.; Muller, D. A.; Xin, H. L.; Abruña, H. D. Spontaneous Incorporation of Gold in Palladium-Based Ternary Nanoparticles Makes Durable Electrocatalysts for Oxygen Reduction Reaction. *Nat. Commun.* **2016**, *7*, 11941.
- (16) Zhu, J.; Yang, Y.; Chen, L.; Xiao, W.; Liu, H.; Abruña, H. D.; Wang, D. Copper-Induced Formation of Structurally Ordered Pt—Fe—Cu Ternary Intermetallic Electrocatalysts with Tunable Phase Structure and Improved Stability. *Chem. Mater.* **2018**, *30*, 5987—5995.
- (17) Xiong, Y.; Xiao, L.; Yang, Y.; DiSalvo, F. J.; Abruña, H. D. High-Loading Intermetallic Pt<sub>3</sub>Co/C Core—Shell Nanoparticles as Enhanced Activity Electrocatalysts toward the Oxygen Reduction Reaction (ORR). *Chem. Mater.* **2018**, *30*, 1532–1539.
- (18) Wang, C.; Sang, X.; Gamler, J. T. L.; Chen, D. P.; Unocic, R. R.; Skrabalak, S. E. Facet-Dependent Deposition of Highly Strained Alloyed Shells on Intermetallic Nanoparticles for Enhanced Electrocatalysis. *Nano Lett.* **2017**, *17* (9), 5526–5532.
- (19) Wang, Y.; Sun, D.; Chowdhury, T.; Wagner, J. S.; Kempa, T. J.; Hall, A. S. Rapid Room-Temperature Synthesis of a Metastable Ordered Intermetallic Electrocatalyst. *J. Am. Chem. Soc.* **2019**, *141* (6), 2342–2347.
- (20) Xiao, W.; Lei, W.; Gong, M.; Xin, H. L.; Wang, D. Recent Advances of Structurally Ordered Intermetallic Nanoparticles for Electrocatalysis. *ACS Catal.* **2018**, *8*, 3237–3256.
- (21) Wang, X. X.; Hwang, S.; Pan, Y.-T.; Chen, K.; He, Y.; Karakalos, S.; Zhang, H.; Spendelow, J. S.; Wu, G. Ordered Pt<sub>3</sub>Co Intermetallic Nanoparticles Derived from Metal—Organic Frameworks for Oxygen Reduction. *Nano Lett.* **2018**, *18*, 4163–4171.
- (22) Prabhudev, S.; Bugnet, M.; Bock, C.; Botton, G. A. Strained Lattice with Persistent Atomic Order in Pt<sub>3</sub>Fe<sub>2</sub> intermetallic Core-Shell Nanocatalysts. *ACS Nano* **2013**, *7*, 6103–6110.
- (23) Bu, L.; Shao, Q.; E, B.; Guo, J.; Yao, J.; Huang, X. PtPb/PtNi Intermetallic Core/Atomic Layer Shell Octahedra for Efficient Oxygen Reduction Electrocatalysis. *J. Am. Chem. Soc.* **2017**, *139* (28), 9576–9582.
- (24) Kang, Y.; Pyo, J.; Ye, X.; Gordon, T.; Murray, C. Synthesis, Shape control, and Methanol Electro-Oxidation Properties of Pt–Zn Alloy and Pt<sub>3</sub>Zn Intermetallic Nanocrystals. *ACS Nano* **2012**, *6*, 5642–5647.
- (25) Zhang, J.; Sasaki, K.; Adzic, R. R. Stabilization of Platinum Oxygen-Reduction Electrocatalysts Using Gold Clusters. *Science* **2007**, 315, 220–222.
- (26) Duchesne, P.; Li, Z.; Deming, C.; Fung, V.; Zhao, X.; Yuan, J.; Regier, T.; Aldalbahi, A.; Almarhoon, Z.; Chen, S.; Jiang, D.; Zheng, N.; Zhang, P. Golden Single-Atomic-Site Platinum Electrocatalysts. *Nat. Mater.* **2018**, *17*, 1033–1039.
- (27) Wang, G.; Huang, B.; Xiao, L.; Ren, Z.; Chen, H.; Wang, D.; Abruña, H. D.; Lu, J.; Zhuang, L. Pt Skin on AuCu Intermetallic Substrate: A Strategy to Maximize Pt Utilization for Fuel Cells. *J. Am. Chem. Soc.* **2014**, *136*, 9643–9649.
- (28) McKale, A. G.; Veal, B. W.; Paulikas, A. P.; Chan, S.-K. Generalized Ramsauer-Townsend effect in extended x-ray-absorption fine structure. *Phys. Rev. B: Condens. Matter Mater. Phys.* **1988**, 38, 10919–10921.
- (29) Yang, Y.; Liu, W.; Wang, Y.; Wang, X.; Xiao, L.; Lu, J.; Zhuang, L. A PtRu Catalyzed Rechargeable Oxygen Electrode for Li-O<sub>2</sub> Batteries: Performance Improvement through Li<sub>2</sub>O<sub>2</sub> Morphology Control. *Phys. Chem. Chem. Phys.* **2014**, *16*, 20618–20623.
- (30) Lu, Y.-C.; Gasteiger, H. A.; Shao-Horn, Y. Catalytic Activity Trends of Oxygen Reduction Reaction for Nonaqueous Li-Air Batteries. *J. Am. Chem. Soc.* **2011**, *133*, 19048–19051.

(31) Yang, Y.; Zhang, T.; Wang, X.; Chen, L.; Wu, N.; Liu, W.; Lu, H.; Xiao, L.; Fu, L.; Zhuang, L. Tuning the Morphology and Crystal Structure of Li<sub>2</sub>O<sub>2</sub>: A Graphene Model Electrode Study for Li-O<sub>2</sub> Battery. ACS Appl. Mater. Interfaces **2016**, *8*, 21350–21357.

- (32) Yang, Y.; Liu, W.; Wu, N.; Wang, X.; Zhang, T.; Chen, L.; Zeng, R.; Wang, Y.; Lu, J.; Fu, L.; Xiao, L.; Zhuang, L. Tuning the Morphology of Li<sub>2</sub>O<sub>2</sub> by Noble and 3d Metals: A Planar Model Electrode Study for Li-O<sub>2</sub> Battery. ACS Appl. Mater. Interfaces **2017**, 9, 19800–19806.
- (33) Aurbach, D.; McCloskey, B. D.; Nazar, L. F.; Bruce, P. G. Advances in Understanding Mechanisms Underpinning Lithium-Air Batteries. *Nat. Energy* **2016**, *1*, 16128.
- (34) Xiao, N.; Ren, X.; McCulloch, W. D.; Gourdin, G.; Wu, Y. Potassium Superoxide: A Unique Alternative for Metal—Air Batteries. *Acc. Chem. Res.* **2018**, *51*, 2335–2343.
- (35) McCloskey, B. D.; Speidel, A.; Scheffler, R.; Miller, D. C.; Viswanathan, V.; Hummelshøj, J. S.; Nørskov, J. K.; Luntz, A. C. Twin Problems of Interfacial Carbonate Formation in Nonaqueous Li—O<sub>2</sub>Batteries. *J. Phys. Chem. Lett.* **2012**, *3*, 997–1001.
- (36) Ottakam Thotiyl, M. M.; Freunberger, S. A.; Peng, Z.; Bruce, P. G. The Carbon Electrode in Nonaqueous Li-O<sub>2</sub> Cells. *J. Am. Chem. Soc.* **2013**, *135*, 494–500.